The Journal of Experimental Biology 209, 5005-5016
Published by The Company of Biologists 2006
doi:10.1242/jeb.02614

Dual leading-edge vortices on flapping wings

Yuan Lu, Gong Xin Shen* and Guo Jun Lai

Full Flow Field Observation and Measurement, Institute of Fluid Mechanics, Beijing University of Aeronautics and Astronautics, Beijing 100083, People's Republic of China

*Author for correspondence (e-mail: gx_shen55@yahoo.com.cn)

Accepted 20 October 2006

Summary

An experimental investigation was performed with two aims: (1) to clarify the existence of the dual leading-edge vortices (i.e. two vortices with the same sense of rotation located close to the leading edge above the leeward wing surface) observed on flapping wings in previous studies; (2) to study systematically the influences of kinematic and geometric parameters on such a vortical structure. Based on a scaled-up electromechanical model flapping in a water tank, the leading-edge vortex (LEV) cores were visualized *via* dye flow visualization, and the detailed sub-structures of LEV were revealed through digital particle image velocimetry (DPIV) with high spatial resolution. Five wing aspect ratios (*AR*) (1.3, 3.5, 5.8, 7.5 and 10), eight mid-stroke angles of attack (α_m) (10–80°), and six Reynolds numbers (*Re*) (160–3200) were examined. In addition, the well-studied case of the fruit fly *Drosophila* was re-examined.

The results confirm for the first time the existence of dual LEVs on flapping wings. The sectional flow structure resembles the dual-vortex observed on non-slender delta wings. Insensitive to *AR*, a dual LEV system such as this could be created when α_m and *Re* reached certain high levels. The primary vortex was attached to the wing, while at the outer wing the minor vortex shed, generating a same-sense vortex behind.

Key words: flapping wing, hovering, flow separation, leading-edge vortex (LEV), electromechanical model, flow visualization, digital particle image velocimetry (DPIV).

Introduction

The leading-edge vortex (LEV), a flow structure responsible for the high-lift generation in insect flight, is well known to both biologists and fluid-mechanists, and has been widely studied both experimentally and numerically (Birch et al., 2004; Ellington et al., 1996; Liu et al., 1998; Wu and Sun, 2004). This type of vortical structure, at certain high Reynolds numbers, is analogous to the spiral conical vortex generated on each leading edge of a delta wing (Birch et al., 2004). However, whereas considerable importance is attached to the force performance and power efficiency of flapping flight (Birch and Dickinson, 2003; Sun and Tang, 2002a; Sun and Tang, 2002b), few studies have addressed the detailed structure of the LEV.

In a recent flow visualization of a robotic wing moving in the motion of dragonfly hovering (Y.L., G.X.S. and W. H. Su, manuscript submitted), we observed that the LEV with intensive spanwise flow did not develop along the leading edge but moved inboard, leaving a space for the formation of a minor vortex outside the primary vortex (see Fig. 1). In fact, a similar LEV pair has been reported in butterfly free flight using smoke-wire visualization (Srygley and Thomas, 2002). This vortical system reminds us of the dual LEV structure on non-slender delta wings, which is defined as the large and small same-sense vortices (the primary vortex and minor vortex, respectively) located close to the leading edge on both sides of the secondary separation in- and outboard, respectively (Gordnier and Visbal, 2003; Taylor and Gursul, 2004). This interesting flow behavior implies that the LEV generated in flapping motions may involve sub-structures, and merit in-depth exploration.

With both visualizations the two vortices were reported to rotate in the same direction, but it is difficult to distinguish them directly from the flow images. In this paper, dye flow visualization and high-resolution DPIV measurements were conducted to reveal the detailed features of the LEV region. Based on the validation of the dual LEV, systematic investigations were performed by altering the kinematic (*Re*, from 160 to 3200, and α_m, from 10 to 80°) and geometric (*AR*, from 1.3 to 10) parameters. The well-known case of the fruit fly was re-examined to see whether the dual LEV had been missed in the previous studies. All measurements were obtained with the robotic wings flapping in the hovering condition.

Materials and methods

Model wing planform

The planform of the simplified model dragonfly wing (*AR*=5.8, *AR*=*R*/*c*; where *R* is model wing length, measured from the translational axis to the wingtip; *c* is mean wing chord length)

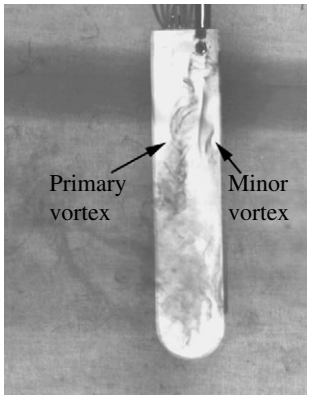

Fig. 1. Dual LEV on a model dragonfly wing (*AR*=5.8), observed in a previous study (Y.L., G.X.S. and W. H. Su, manuscript submitted for publication). The wing was at mid-downstroke with mid-stroke angle of attack α_m=60°.

served as the basis for producing the other model wings, forming a range of five *AR* (1.3, 3.5, 5.8, 7.5 and 10, see Fig. 2). The range of aspect ratios selected here not only covered the lowest and highest aspect ratios of insect wings (Dudley, 1990; Ellington, 1984a), but also included the case of a rotary wing. The wing planform used here was not only for simplification, but also to eliminate any geometric interference, such as the curved leading edge, from the LEV structure. Mechanical constraints meant the model wings were mounted on the tip of the rotational shaft, and the wing bases were 46 mm away from the translational axis (denoted as OT in Fig. 3A). All model wings were fabricated from 1 mm flat aluminum sheets to minimize the thickness effect (*c*-based normalized thickness 5%) and to allow sufficient strength and rigidity. Model wings with *AR* ranging from 1.3 to 7.5 mm thick all had an effective wing length (*r*, measured from the model wing base to the tip; see Fig. 2) of 104 mm, rendering *R*=150 mm. The narrowest wing (*AR*=10) had *r*=154 mm, so *R*=200 mm. In addition, to re-examine the case of the fruit fly wing, we used a model wing with the same planform as fruit fly *Drosophila* (*AR*=3.1, *R*=150, *r*=129).

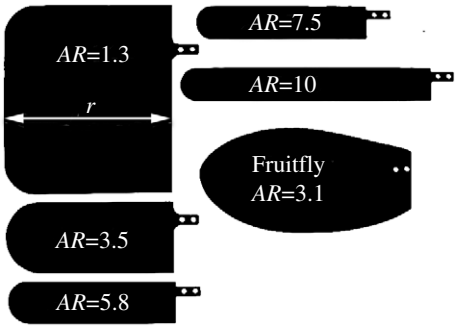

Fig. 2. Model wing planforms with a range of aspect ratios (*AR*). Except for the wing with *AR*=10 and the model fruit fly wing, which had an effective wingspan *r* of 154 mm and 129 mm, respectively, for all the others *r*=104 mm.

Kinematics and simulation

The flapping kinematics included two degrees of freedom (d.f.): translation and rotation. As sketched in Fig. 3, translation is the azimuthal rotation of the wing about the translational axis OT, and rotation is the supinating/pronating rotation about the axis OZ (located at 1/4 wing chord from the leading edge, denoted in Fig. 3 as a thick black line). OD and OU in Fig. 3 are two translational extreme positions, and they define the horizontal stroke plane and the stroke amplitude Φ. The translational angle ϕ varied as the cosine function (Ellington, 1984b):

$$\phi = 0.5\Phi[1 - \cos(2\pi t/T)] \, . \quad (1)$$

The rotational angle ρ (ρ=90–α°, where α = angle of attack; ρ_m = the maximal rotational angle) varied as a simple harmonic function when the wing was undergoing rotation, but remained constant when the wing was purely translating. The duration of rotation Δ*Tr* was fixed at 0.2*T*, thus the rotational function in one period was:

$$\rho = \begin{cases} \rho_m \sin(\pi t/\Delta T_r) & 0 \leqslant t < 0.1T \\ \rho_m & 0.1T \leqslant t < 0.4T \\ \rho_m \cos[\pi(t-0.4T)/\Delta T_r] & 0.4T \leqslant t < 0.6T \\ \rho_m & 0.6T \leqslant t < 0.9T \\ -\rho_m \cos[\pi(t-0.9T)/\Delta T_r] & 0.9T \leqslant t < T \, . \end{cases} \quad (2)$$

The kinematic curves are plotted in Fig. 3B. In this study, adjusting ρ_m could achieve different values for α_m; altering *T* (or stroke frequency *n*) would yield various *Re* values [$Re=U_t c/\nu$, where U_t = mean wingtip translational velocity; ν = kinematic viscosity; *n* = stroke frequency (Ellington, 1984b); here, since $U_t=2\Phi nR$, $Re=2\Phi nRc/\nu$].

The flapping motions were mimicked *via* a self-designed electromechanical system, which contained two servo motors (Maxon Corp., Sachseln, Switzerland) linked to a controller (Nyquist Corp., Eindhoven, Holland) controlled by the self-written software. The two motors output the translation and rotation, respectively, when a given motion was discretized and input into the personal computer. To examine the simulation quality, we sampled three sequential periods of the output motions and compared them with the ideal data. The calculated correlation coefficients (using the correlation coefficient function in Matlab 7.0.4) of translation and rotation were 0.9847 and 0.9305, respectively, validating our kinematic simulation.

Dye flow visualization

Dye flow visualization offers integral pictures of the flow structures, and always serves as a reference for the DPIV measurement. In this study, dye visualization was conducted in a water tank of dimensions 600 mm×400 mm×400 mm (length×width×depth). The electromechanical system was mounted on the top of the tank. The LEVs were visualized *via* dyes released from a single tube (diameter roughly 1 mm), placed at the node of the leading edge and vertical to the spanwise direction so as to minimize the impact of dye

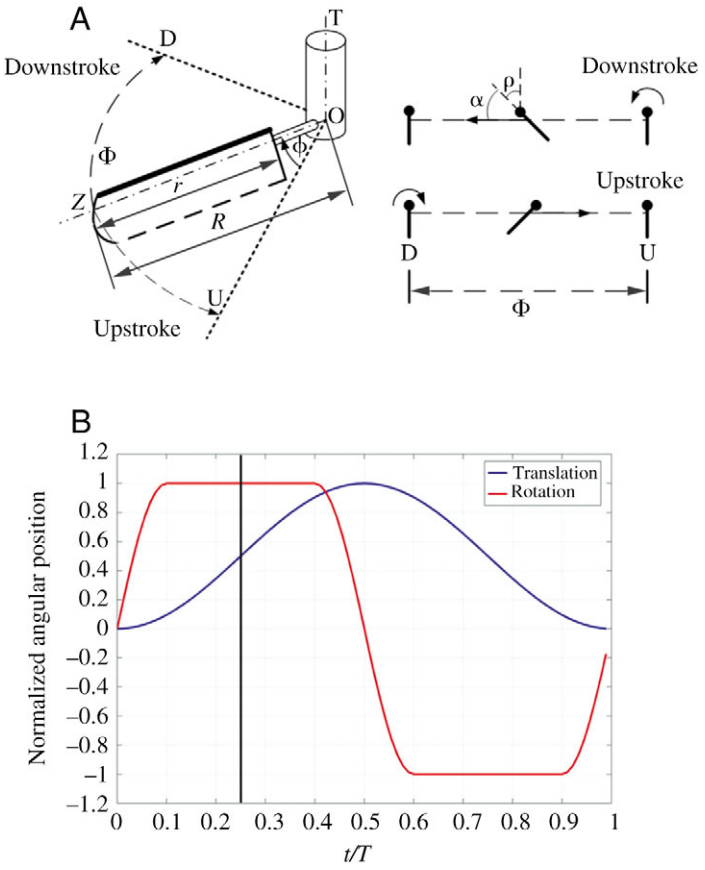

Fig. 3. Sketch of flapping motion in hovering. (A) Left: spatial configuration of the flapping motion of a model wing. The thick black line denotes the leading edge; OT, translational axis; OZ, rotational axis; OD and OU, the translational extreme positions; *R*, model wing length; *r*, effective model wing length; Φ, stroke amplitude; ϕ, instantaneous translational angle. Right: the motion of a section of the wing. α, instantaneous angle of attack; ρ, instantaneous rotational angle (ρ=90–α°); black thick line denotes wing section and solid-dot, the leading edge. (B) The kinematic curves over one period. The translational and rotational angular positions are normalized using Φ and ρ_m (maximal rotational angle), respectively. The black line at *t*/*T*=0.25 denotes the DPIV triggering phase.

releasing speed on the spanwise flow (Fig. 4). A commercial digital video (frame rate 25 frames s^{-1}) was used for recording. Two perspectives, i.e. viewing down from the top and horizontally along the stroke plane, were used to obtain representative flow images when the wing was traveling with different α_m values. The water was originally static, representing the hovering condition. All flow pictures were recorded after the wing had moved for more than five periods to ensure the establishment of the flow field.

DPIV measurement

DPIV measurements were also performed in the water tank, in which the water was seeded with hollow glass beads of diameter 1–5 μm. The dye-tubes on the model wings used in the dye visualizations were all removed, canceling any potential

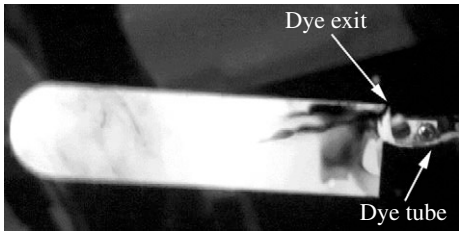

Fig. 4. Flow visualization by the dye release method.

interference. A 2 mm thick laser-sheet was created by a dual-pulse Nd-Yag laser system (maximum of 200 mJ $pulse^{-1}$, LABest, Beijing, China). A frame-straddling CCD camera (1920 pixel×1080 pixel, Red Lake, San Diego, CA, USA) equipped with a lens (Micro Nikkor 105mm f/2.8, Nikon, Tokyo, Japan) was employed to achieve sufficient spatial resolution. Another CCD camera with resolution of 1008 pixel×1018 pixel (Red Lake) was used to capture the global flow field that contained both the leading- and trailing-edge vortices. The CCDs were positioned perpendicular to the light sheet. The electromechanical system was mounted on a positioning translation system (the translating direction was perpendicular to the light-sheet) on the top of the tank, and thus it was possible to measure at different spanwise locations without displacing the DPIV system. The initial positions of the wings were well adjusted, ensuring that the spanwise direction of the wing was perpendicular to the light sheet at mid-stroke. Equipped with a digital delay/pulse generator (DG 535, Stanford Research System Co., Sunnyvale, CA, USA), the laser pair was triggered and the image pair was recorded when the wing arrived exactly at the mid-downstroke position (*t*=0.25*T*). Several laser-pulse separations with a range of 2–8 ms were applied to fit different *Re* situations. In each case, over 15 periods were sampled and averaged, excluding the first five periods (to avoid the 'start-up effect'). Cross-correlation and vorticity calculations were completed using software developed by the authors. In the cross-correlation procedure, an interrogation area of 32 pixel×32 pixel with a searching step of 16 pixel was used, achieving 8100 vectors in total. Typical velocity vectors are shown in Fig. 5A. The DPIV data were post-processed through Tecplot 10. The overall DPIV arrangement is depicted in Fig. 5B.

Since only two-dimensional PIV was applied in this study, the sectional flow fields should be treated with caution for the following reasons. (1) The streamlines presented here are neither the actual stream patterns, nor their projection onto the laser-sheet plane – they should only be called sectional streamlines. However, they are helpful in providing some flow field information, e.g. the distribution of the critical points. (2) If the plane of interest is not vertical to the local vortex axis, the planar flow field topological structure may change (Dallmann et al., 1995). Thus, the absence of a focus in a vorticity-condensed region alone may be not sufficient to rule

out the existence of a vortex; this case did indeed occur in our study and will be analyzed below.

Results

Validation of dual LEV structure

Validation based on both flow visualization and DPIV, was performed as a first step to clarify the rotational senses of the two vortices. Previously, the dual LEV was observed in the downstroke when the model dragonfly wing (*AR*=5.8) was moving with the pattern of dragonfly hovering (non-symmetrical hovering, α_m for down- and upstrokes = 60° and 30°, respectively) (Norberg, 1975). In the present study, we controlled the model wing so that it flapped symmetrically using α_m=60° for both down- and upstrokes. Φ was set to 60°, the same for the dragonfly. *n* was set to 0.2 Hz so that *Re*=1624, a value within the range of dragonfly hovering (Dudley, 2000).

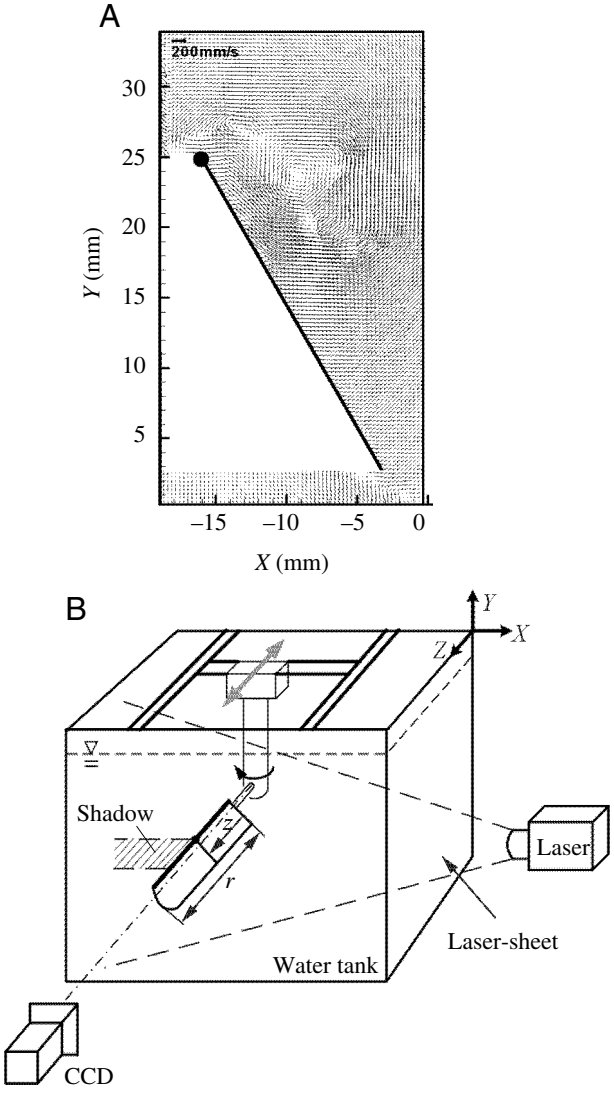

Fig. 5. DPIV setup. (A) Typical velocity vectors. The black thick line denotes wing section and the solid-dot the leading edge. The white area in front of the wing represents the shadow due to the nontransparency of the aluminum wing. Scale bar, 200 mm s^{-1}. (B) Sketch of DPIV arrangement. The large gray arrow denotes the positioning translation of the model system. *X* and *Z* are two axes in the horizontal plane, while *Y* heads vertically away from the ground; *z*, the distance between the wing-base and the laser-sheet; *r*, the effective wing length. The laser-sheet and CCD were always perpendicular and parallel to *Z*, respectively.

Flow visualization

Fig. 6 shows the LEV core evolution during downstroke (since the strokes were symmetrical during down- and upstrokes, we only present here the downstroke image sequence). It can be seen that two dye-concentrated lines close to the leading edge were spiraling towards the wingtip. The short one (the minor vortex) was always along the leading edge, while the inboard long one (the primary vortex) was deviating from the leading edge. This result, to certain extent, confirms our finding of the dual LEV in the prior experiment, and it also indicates that the interference of the rotational shaft and linkage (see Fig. 1), which potentially could have certain influence, evidently did not change the LEV structure. During the later half of the stroke when the wing was decelerating, the primary vortex broke down at roughly 0.35*r*. By contrast, the minor vortex became loose in structure (Fig. 6C). Vortex breakdown (or burst) is a dramatic change at some points of the LEV, including axial speed drop, vortex core expansion (Leibovich, 1984). The effect of the vortex breakdown is to reduce the lift of the wing.

DPIV measurement

DPIV measurement can be used to clarify the rotational senses of the two vortices and is capable of revealing the local detailed flow structure. The following DPIV measurements were all conducted at mid-downstroke (*t*=0.25*T*).

First, a section at 0.29*r*, where the two vortices could be distinguished easily, was studied. As shown in Fig. 7A, two vorticity-condensed regions with the same sign (negative, blue contour) located above the leeward surface near the leading edge are conspicuous. According to the spatial distribution shown in the visualization picture at 0.25*T* (Fig. 6B), the larger inboard vortex corresponded to the primary vortex, while the

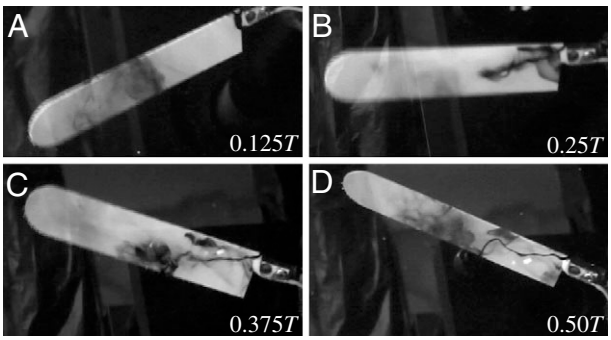

Fig. 6. (A–D) Dye flow visualization showing the dual LEV evolution over one stroke (*T*; *AR*=5.8, α_m=6°, Φ=60°, *Re*=1624).

outboard counterpart was in accordance with the minor vortex. Facilitated by sectional streamlines, two foci can be identified in the centers of the two vorticity-concentrations, demonstrating the vortex nature of these two regions. As a result, the first evidence of the dual LEV structure on a flapping wing is presented. In addition, the secondary separation with opposite vorticity (yellow contour) can be detected between the two vortices just above the wing surface. These three vorticity regions constitute the basic structure of the dual LEV, reminding us of the dual-vortex structure on non-slender delta wings (Gordnier and Visbal, 2003; Taylor and Gursul, 2004). Note in Fig. 7A that a small separation layer with negative vorticity locates outboard from the minor vortex at the leading edge, where the sectional streamlines bend dramatically but form no focus. This layer can also be found in all spanwise locations in Fig. 7B. Since it is the most outboard separation structure, we name it the outboard separation.

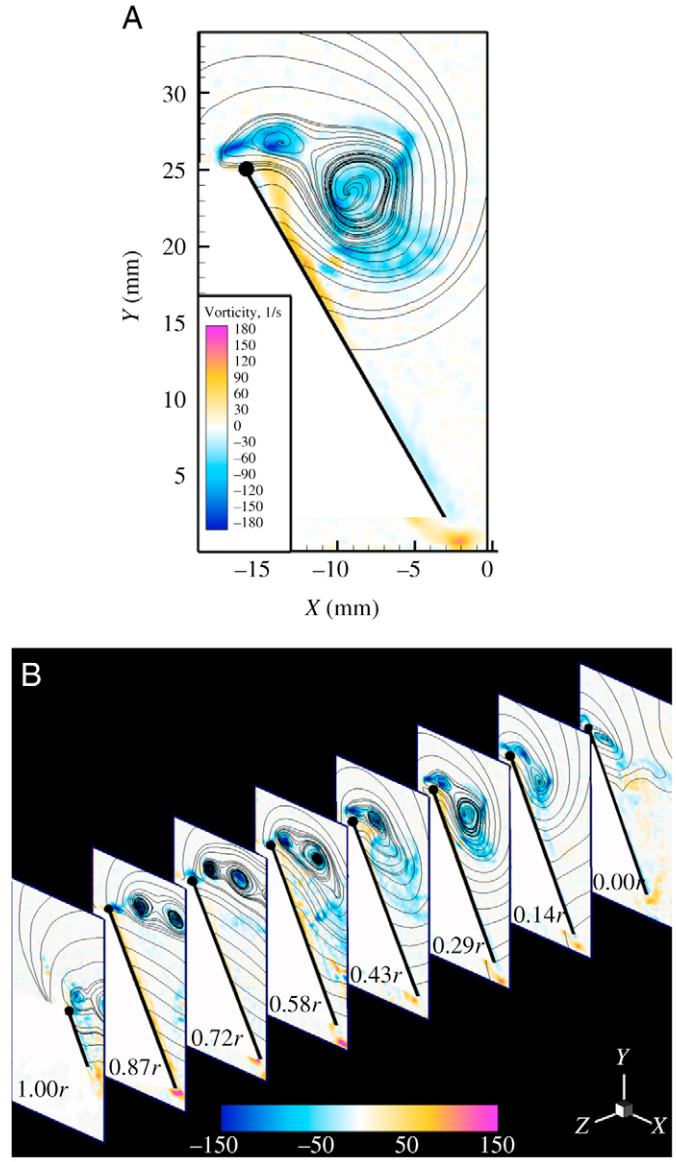

Fig. 7. DPIV results at mid-downstroke (0.25*T*, the same phase as Fig. 6B). (A) A typical result at 0.29*r* (effective model wing length *r*=104 mm). The black thick line denotes wing section and the solid-dot the leading edge. Sectional streamlines are plot. The pseudocolor contour represents the spanwise vorticity. (B) Sectional flow fields at different spanwise locations. The slices were spaced by 15 mm and were all perpendicular to the spanwise direction. Plot representation as in A.

We estimate that there are probably several reasons why the dual LEV was missed in previous experimental and numerical studies. (1) Improper tracer released location and the use of discrete tracers such as bubbles may prohibit sufficient tracers from entering and visualizing the minor vortex (Birch et al., 2004; Ellington et al., 1996). (2) The spatial resolution of CFD and PIV in prior studies may have been inadequate to reveal the fine flow structures (Liu et al., 1998; Maybury and Lehmann, 2004). (3) α_m in prior studies was in the range of 40–45°, and the PIV laser-sheets were always vertical to the spanwise direction; at this relatively low α_m the primary vortex could not be illustrated by sectional streamlines as the local vortex axis deviated from the spanwise direction (Birch et al., 2004; Dallmann et al., 1995), which will be shown below.

Further, because the flow field at the outer wing could not be visualized *via* this dye method, DPIV measurements were conducted along the spanwise direction from the wing-base to the tip with a 15 mm separation. It is clear in Fig. 7B that the vortex pairs are remarkable at all spanwise locations except at the wing-base. However, it should be emphasized again that the primary vortex and minor vortex in the dual LEV system refer to those located on both sides of the secondary separation in- and outboard, respectively. In this sense, the vortex pairs in Fig. 7B, which can be identified as dual LEV, are those within the range 0–0.58*r*. The main reason for the absence of foci in the primary vortex region at 0.43*r* and 0.58*r* is the relatively large deviation of the local vortex axis from the spanwise direction (or the laser-sheet normal), which changed the sectional topological structure (Dallmann et al., 1995). Although the primary vortex increased in size along the spanwise direction (showing a conical shape) and showed severe vorticity diffusion at the outer wing, it remained attached to the wing surface.

Questions on the foci pairs at the outer wing from 0.43*r* to1.00*r* still remain, however; what are they, and how did they form? Unfortunately, these structures could not be elucidated through current dye visualization. We estimate that the minor vortices were undergoing shedding, leaving a same-sense vortex generated behind.

Systematic studies by varying the kinematic and geometric parameters

In the following sections, the visualization pictures at mid-downstroke and DPIV results at 0.29*r* are presented.

The effect of α_m

α_m was altered from 10° to 80° with a separation of 10°. The model dragonfly wing (*AR*=5.8) was still used, and the same

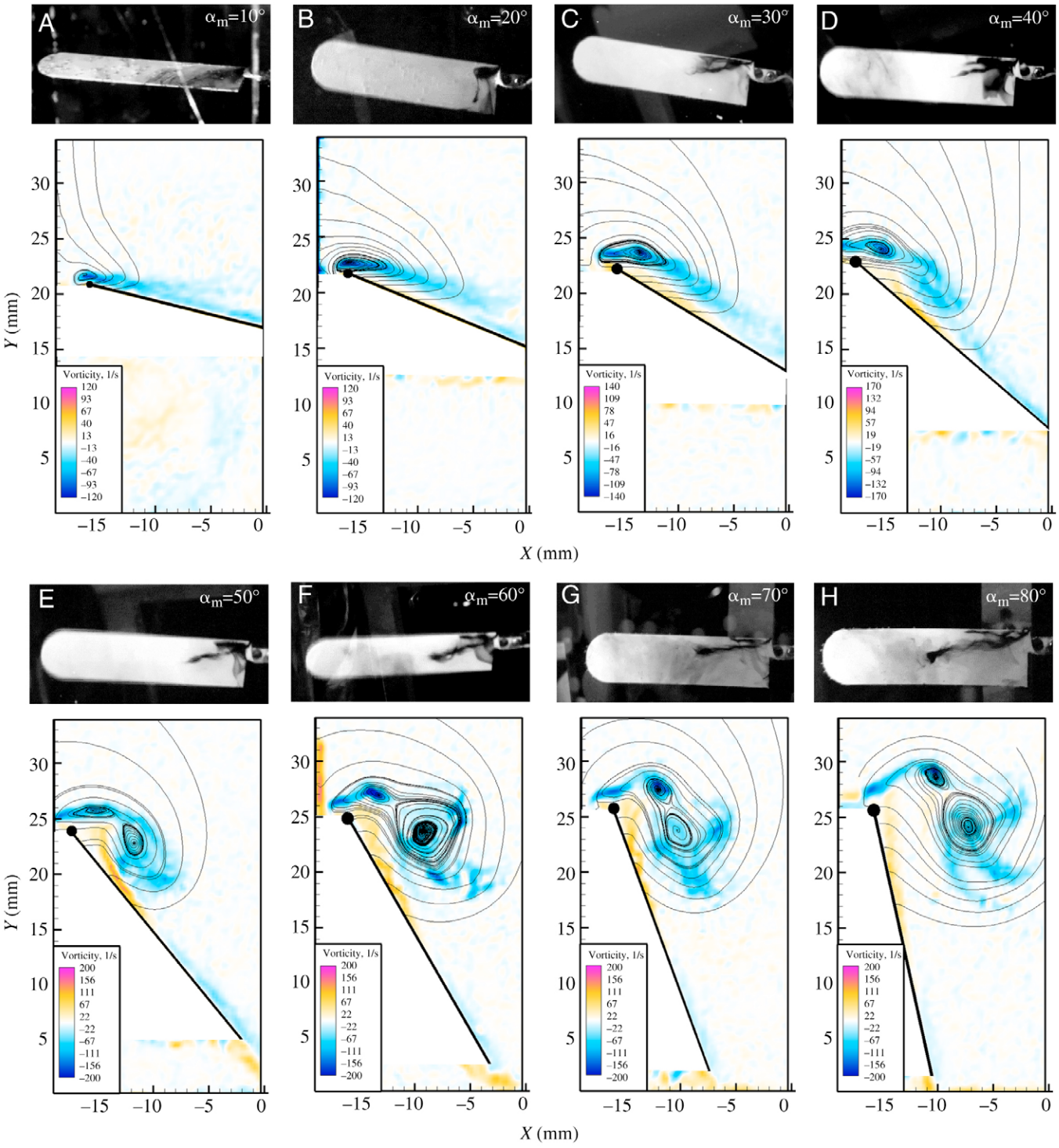

Fig. 8. Dual LEV in various α_m conditions (*AR*=5.8, Φ=60°, *Re*=1624). Visualization pictures were captured at mid-downstroke (0.25*T*). Sectional flow fields at 0.29*r* were measured *via* DPIV at the same phase as the visualization pictures. Plot representation as in Fig. 7A.

stroke amplitude and Reynolds number were retained (Φ=60°, *Re*=1624).

The results are shown in Fig. 8. When the wing was translating with a small α_m (below 30°), there was only a thin vorticity layer covering the leeward surface of the wing, and only a weak vortex that showed no spiral structure was created (Fig. 8A,B). When α_m reached 30° (Fig. 8C), two branches of concentrated LEV with considerable spanwise flows were generated. However, the LEV vorticity layer was still well connected, allowing the two vortices to interact easily with each other; such an interaction can be detected from the visualization picture in Fig. 8C as the fact that the dyes

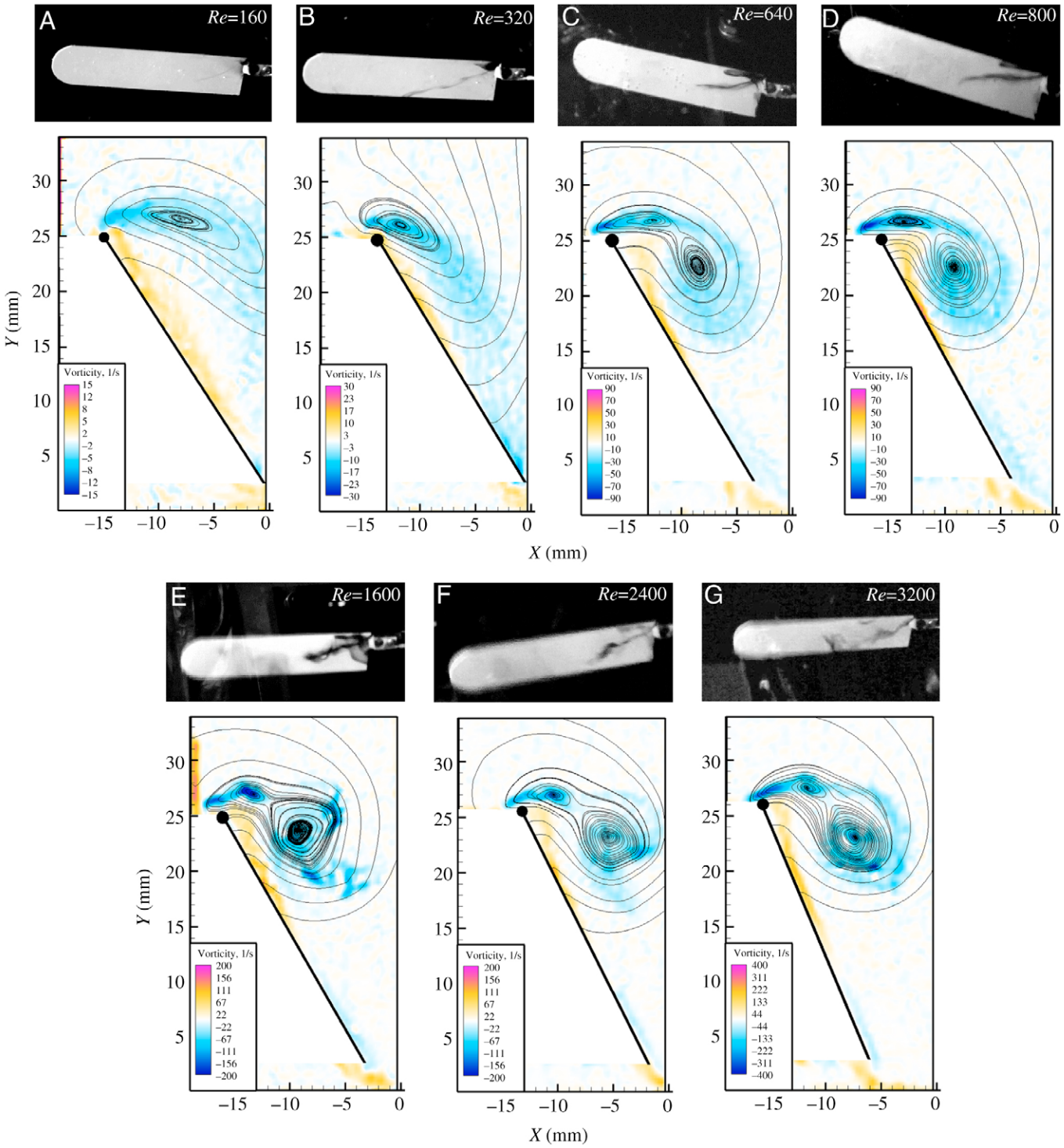

Fig. 9. Dual LEV in various *Re* conditions (*AR*=5.8, α_m=60°, Φ=60°). Visualization pictures were captured at mid-downstroke (0.25*T*). Sectional flow fields at 0.29*r* were measured *via* DPIV at the same phase as the visualization pictures. Plot representation as in Fig. 7A.

belonging to the minor vortex were being sucked by the primary vortex. The sectional streamlines fail to show the primary vortex, because the local vortex axis considerably deviated from the spanwise direction (Dallmann et al., 1995). Similar phenomena for possibly the same reason occurred when α_m=40° (Fig. 8D). The two results may explain one of the reasons for missing dual LEV in prior studies, in which α_m was in the range 40–45° and the sampling planes such as the PIV laser-sheet were always vertical to the spanwise direction (Birch et al., 2004).

At a certain level (α_m reached 50°), both the vorticity of LEV and secondary separation were enhanced. More significantly,

the LEV area was no longer connected but separated into two in- and outboard sub-regions, which were in accordance with the primary and minor vortex, respectively (Fig. 8E). Further increasing α_m (to 60° and larger), even though the two LEVs still appended above the wing surface, they were more distant from the wing. As a consequence, the two LEVs and the secondary separation all became weaker (Fig. 8F–H). The outboard separation (defined above) can also be observed in the DPIV images when α_m was sufficiently large (α_m reached 60°, see Fig. 8F–H). However, flow visualizations did not capture this structure, possibly because it was not a vortex in nature.

In sum, dual LEV existed when the wing flapped with an α_m not less than 30°. Additionally, increasing α_m, the distance between the dual LEV and leeward wing surface was enlarged, and the two LEVs and the secondary separation all became weaker.

The effect of Re

Again, the model dragonfly wing and flapping pattern (α_m=60°, Φ=60°) were applied, but the stroke frequency *n* was altered from 0.02 to 0.4 Hz to achieve a set of *Re* ranging from 160 to 3200.

At very low *Re* of 160 (roughly the *Re* of hovering fruit fly), there was a small crescent-like region of negative-sign vorticity near the leading edge at a considerable distance from the wing. A focus with a loose structure was in this region (Fig. 9A). The visualization picture in Fig. 9A reveals that only a very thin dye line was developing outboard to the trailing edge, while it failed to show a compact spiral structure. Compared with the case of *Re*=160, when *Re*=320, the vortical layer was closer to the wing and was stronger. Though the dye line at the primary vortex position was thicker and showed some spiral appearance, it still failed to thoroughly roll up into a concentrated vortex core (Fig. 9B). Also in Fig. 9B, the failure to represent this spiral structure *via* sectional streamlines could also be attributed to the larger deviation of the local vortex axis from the spanwise direction. Further increasing *Re* (from 640 to 3200), the negative vorticity-concentration rolled more tightly and finally divided into two individual regions, resulting in the formation of two concentrated vortices (Fig. 9C–G). Meanwhile, the secondary separation was strengthened. At the highest levels (*Re*=2400–3200), the primary vortex broke down at mid-stroke, earlier than for the lower *Re* cases (Fig. 9F,G). Unlike the α_m situations, the relative positions of the LEVs and the leeward wing surface did not change dramatically as *Re* increased. Additionally, the outboard separation became more remarkable when *Re* was increased.

In general, dual LEV existed only when *Re* reached the level of roughly 640.

The effect of AR

Aspect ratio (*AR*) is a simple but important geometric variable characterizing the shape of a wing. A range of *AR* from 1.3 to 10 was studied to see whether and how the geometric factor affected the dual LEV. The α_m was set to 40° to fit the common situation in hovering insects (Ellington, 1984b).

First, clarification of the dual LEV in butterfly free flight (Srygley and Thomas, 2002) was conducted. A model wing with *AR*=1.3 [the same as butterfly *Morpho peleides* Butler (Dudley, 1990)] was mounted on the flapper and moved with Φ of 150°. *n* was adjusted to 0.05 Hz, so that *Re*=4504, within the range of butterfly flapping flight (Dudley, 1991). From the visualization picture in Fig. 10, one can see a similar dual LEV pattern as discussed previously. Two same-sense vortices are also evident in the DPIV image. Therefore, dual LEV was confirmed for the low *AR* flapping wing, in addition to the condition with large *AR*.

Next, we complemented the other *AR* cases to gain more systematic insight into the effect of *AR*. As an intermediate case, *AR*=3.5 was conducted (Φ=150°, *n*=0.05 Hz, *Re*=1673). Again, a similar flow phenomenon was obtained. *AR* was further increased to 7.5 and then to the extreme situation of 10, into the level of rotary wing. In these two experiments, Φ=60°, following the manner of the dragonfly case (*AR*=5.8). *n* was 0.25 Hz and 0.2 Hz, respectively, so *Re* was at the level of 1600 (*Re*=1561 and 1666 for the cases of *AR*=7.5 and 10, respectively). Surprisingly, the dual LEV structure was also evident on these very narrow wings, as with the lower *AR* cases. The failure to illustrate the primary vortex in the case of *AR*=5.8 and 7.5 *via* sectional streamlines could be also due to the large deviation of local vortex axis from the spanwise direction (Dallmann et al., 1995).

In general, the dual LEV system on a flapping wing was not sensitive to *AR*.

The case of fruit fly wing

The famous fruit fly case (*AR*=3.1) was restudied. *Re* was adjusted to a relatively high value of roughly 1889 (α_m=40°, Φ=150°, *n*=0.05 Hz) to allow the formation of concentrated LEV with intensive spanwise flow (Birch et al., 2004).

Again, the dual LEV was obvious (Fig. 11A,B). Considering the fruit fly wing emphasizes a curved leading edge, this experiment further indicates that the impact of the geometric factors is not as significant as the kinematic counterparts. The spanwise flow structures were also investigated (Fig. 11C), with similar results: the minor vortex at the outer wing was shed, resulting in a same-sign vortex created behind. Compared with the case of dragonfly wing with large *AR* (=5.8), the primary vortex on fruit fly wing diffused conspicuously only near the wingtip, showing a more stable structure.

Discussion

The formation of dual LEV

The LEV on a flapping wing contains sub-structures that are very similar to the flow structures on non-slender delta wings (Gordnier and Visbal, 2003; Taylor and Gursul, 2004).

In the domain of delta wing, there have been several explanations to describe the formation of the dual LEV. For instance, Gordnier and Visbal stated that: "*The development of the second primary vortex results from the impingement of the secondary separated flow on the primary shear layer splitting*

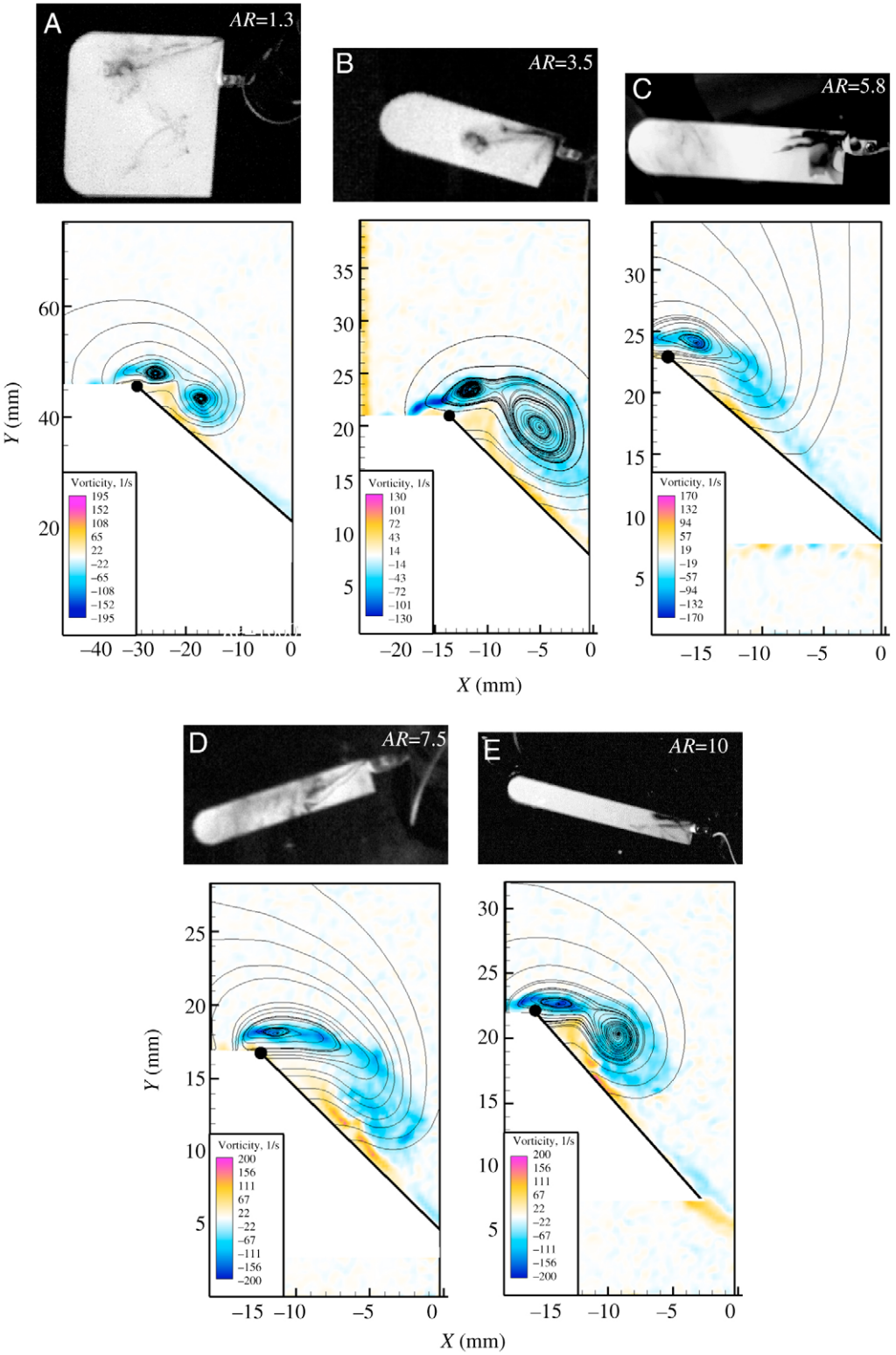

Fig. 10. Dual LEV in various *AR* conditions (α_m=40°). Visualization pictures were captured at mid-downstroke (0.25*T*). Sectional flow fields at 0.29*r* were measured *via* DPIV at the same phase as the visualization pictures. Plot representation as in Fig. 7A.

it into two same-sign vortices" (Gordnier and Visbal, 2003), which stressed the role of the secondary separation. Taylor and Gursul stated that: "*With increasing Reynolds number, the significant interaction between the boundary layer and primary vortex results in this dual vortex structure*" (Taylor and Gursul, 2004), which emphasized the boundary-vortex interaction.

Henning et al. suggested that "*The topological flow structure changes on the one hand because the cone angle of the primary vortices is greater than this of a highly swept delta wing and on the other hand because the vorticity in the vortex core is not as strong*" (Henning et al. 2005), which mentioned the effect of primary vortex cone angle and its relatively low vorticity.

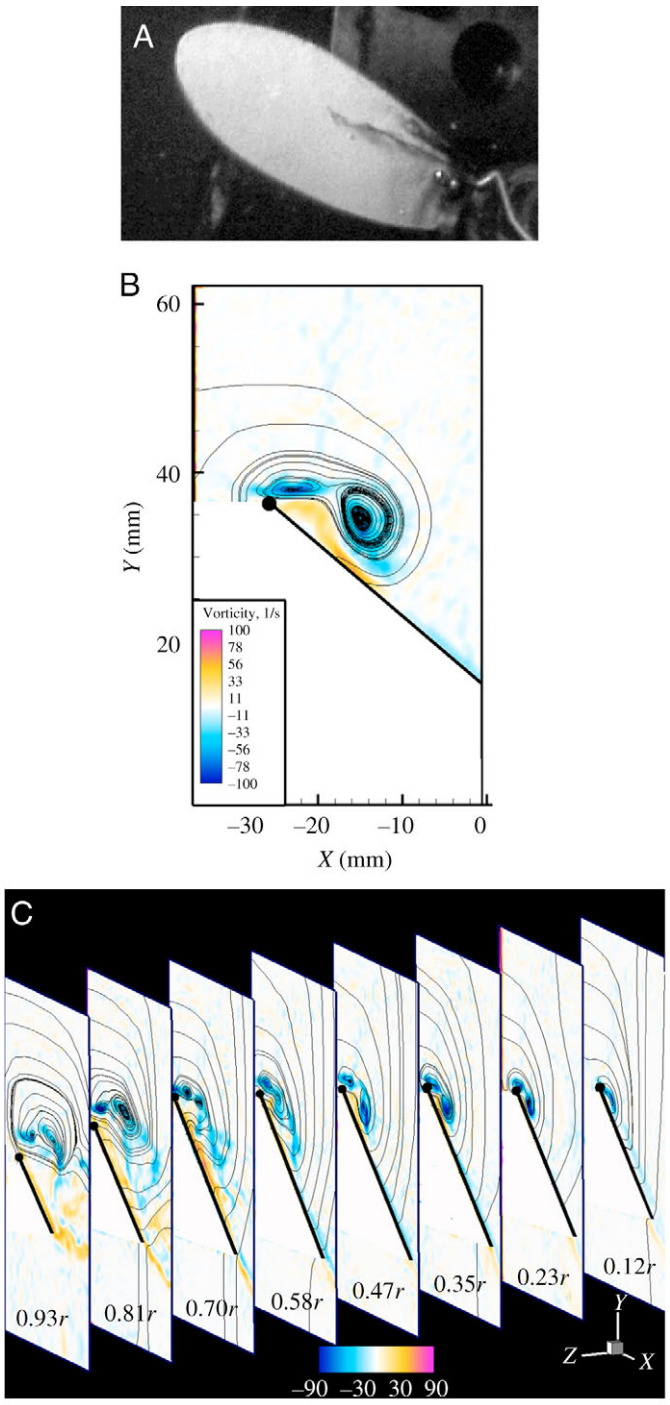

Fig. 11. Dual LEV on model fruit fly wing (*AR*=3.1, α_m=40°, Φ=150°, *Re*=1889). The results were captured or measured at mid-downstroke (0.25*T*). (A) Dye visualization picture. (B) DPIV result at 0.35*r* (*r*=129 mm). Plot representation as in Fig. 7A. (C) Sectional flow structures at different spanwise locations. The DPIV slices were spaced by 15 mm.

Return to the current issue of flapping wing, neither of the above possibilities could be ruled out. Our preliminary estimation was that the secondary separation may play an active role in the minor vortex formation: while the separated boundary layer at the leading edge was rolling up to form the primary vortex, the induced secondary separation simultaneously induced the outboard separated flow to roll up into the minor vortex. However, the secondary separation alone might not be enough, because in some conditions the dual LEV was remarkable while the secondary separation was very weak. For instance, when α_m=80°, even near the wing-base the primary vortex was distant from the wing, resulting in a feeble secondary separation (Fig. 8H). Also at the outer wing, especially near the wingtip where the primary vortex diffused dramatically, a strong secondary separation had no chance to be induced (Fig. 7B). Therefore, we estimate that the negative-sign vorticity layer outboard from the minor vortex, i.e. the outboard separation, could potentially play certain role in transporting vorticity to the minor vortex, especially when the secondary separation no longer had substantial influence.

In addition, whereas the present study is based on hovering condition, the previous observation of free butterfly flight (Srygley and Thomas, 2002) suggested that the existence of the dual LEV structure may be beyond the hovering domain.

The influences of kinematic and geometric parameters on dual LEV

According to the above experimental facts and analyses, it can be concluded that dual LEV structure on a flapping wing can be created when α_m and *Re* reach a certain level, i.e. $\alpha_m \geqslant 30°$, $Re \geqslant 640$, implying that kinematic parameters place a certain impact on the dual LEV generation. On the other hand, dual LEV not only existed in a wide range of aspect ratios, but also on a wing with a curved leading edge, suggesting that the effect of geometric variables is relatively slight. Note that on a delta wing the dual-vortex structure exists only within a range of sweepback, angle of attack and Reynolds number (Gordnier and Visbal, 2003; Taylor and Gursul, 2004), the universal existence of flapping wings' dual LEV is a particularly interesting phenomenon. Probably, such a vortical system may be a basic flow structure of flapping wings.

The flow structures along the spanwise direction

The flow field at different spanwise locations was investigated based on DPIV for both the large *AR* dragonfly wing and low *AR* fruit fly wing. In both cases, even though unstable and diffused at the outer wing due to the reverse pressure gradient near the wingtip (the 'wingtip effect'), the primary vortex remained attached on the leeward wing surface. Nevertheless, at the outer wing the minor vortex showed

shedding appearance, leaving a same-sense vortex formed behind.

The complexity of the three-dimensional vortical structure shown in present study, which involves the multiple-vortex system and different flow behaviors along the spanwise direction, may be beyond our previous knowledge. Considering the technical deficiency of the employed dye method and two-dimensional DPIV measurements, in-depth study on the outer wing flow pattern is necessary.

Global topological structure of the sectional flow field

Topological analysis has played an important role in the study of three-dimensional separated flows (Su et al., 1990). The complex nature of the flow field around a flapping wing, for example the high time-dependency, may be beyond the theoretical framework of the topological method. Nevertheless, with caution in mind, the topological analysis is still helpful in shedding some light on the skeleton of the global flow field. In this sense, according to the above results revealing the dual LEV details and a DPIV image capturing the full flow field that contained both the leading- and trailing-edge vortices (see Fig. 12A), the global topological structure of the sectional flow field is presented.

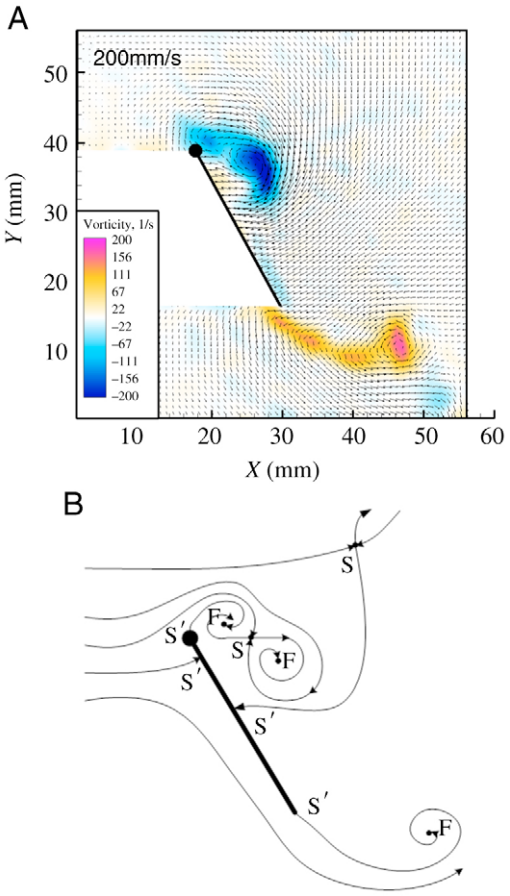

Fig. 12. Global sectional flow structure. (A) DPIV result at 0.29*r* at mid-downstroke (*AR*=5.8, α_m=60°, Φ=60°, *Re*=1624). Plot representation as in Fig. 7A; velocity vectors are shown. The in- and outboard blue vorticity concentrations correspond to the primary and minor vortices, respectively. The yellow and pink vorticity region behind the trailing edge is the shed trailing-edge vortex. Scale bar, 200 mm s^{-1}. (B) Conjectured topological structure of the sectional flow field. F, focus; S, saddle; S′, semi-saddle.

Although the flow fields in front of the windward surface were lost owing to the nontransparency of the aluminum wing, the flow details in the boundary layer were overshadowed by the laser reflection, and the critical points at far-field were out of the sampling window, they can still be deduced indirectly based on the topological rule: for a continuous vector field cut by a simply connected body, the number of nodes equals to the number of saddles (including semi-saddles on the body) minus one (Perry and Chong, 2000). The topological structure of the global sectional flow field is sketched in Fig. 12B. There are three foci (F) in total (two belong to the dual LEV and the rest to the shed trailing edge vortex), two saddles (S; one connects the dual LEV and the other is in the far-field) and four semi-saddles (S′; on the wing windward and leeward surfaces). Note that topologically, node and focus are equivalent, the relation of the number of foci and saddles is 3–(2+4×1/2)=–1, obeying the topological rule.

Concluding remarks

In this experimental study, the dual LEV is confirmed for the first time on flapping wings. Insensitive to aspect ratio, such a vortical system could be created when α_m and *Re* reached a certain high level. Whereas the present experiments were performed in the hovering condition, considering the observation of Srygley and Thomas (Srygley and Thomas, 2002), the dual LEV may also probably exist in other free flight conditions such as forward flight. In general, dual LEV may be a basic flow structure of flapping wings.

The primary vortex did not develop along the leading edge but moved inboard. Although diffused at the outer edge, it remained attached to the leeward wing surface. On the other hand, the minor vortex formed along the spanwise direction, but shed at the outer wing, leaving a same-sense vortex created behind. Despite the existence of the sub-structures, their contributions to the general aerodynamics may be minor compared with those generated by the attached primary vortex. As far as the minor vortex formation is concerned, the secondary and outboard separations may both play active roles, and the outboard separation probably serves as a vorticity source in the shedding process of the minor vortex. Nevertheless, the present visualization and DPIV can hardly provide more information on the 3-D structure of this complex multiple-vortex system. Therefore, further visualization works that can effectively elucidate the flow situation at the outer wing, using 3-D PIV techniques such as stereoscopic DPIV (DSPIV) equipped with proper vortex identification method, and systematic study covering different phases in a stroke period, are desirable to understand the mechanism of the dual LEV formation and the global flow structure.

List of symbols

AR	aspect ratio (R/c)
c	mean wing chord length
DPIV	digital particle image velocimetry
LEV	leading edge vortex
n	stroke frequency
r	effective model wing length
R	model wing length
Re	Reynolds number
t	time
T	stroke period
U_t	mean wingtip translational velocity
α	angle of attack
α_m	mid-stroke angle of attack
ϕ	instantaneous translational angle
Φ	stroke amplitude
ρ	instantaneous rotational angle
ρ_m	maximum rotational angle
ν	kinematic viscosity

We express appreciation to the anonymous referees for the insightful comments. We also thank Wen Han Su for the helpful discussion. This work is supported by Chinese Natural Scientific Foundation CNSF10472011.

References

Birch, J. M. and Dickinson, M. H. (2003). The influence of wing–wake interactions on the production of aerodynamic forces in flapping flight. *J. Exp. Biol.* **206**, 2257-2272.

Birch, J. M., Dickson, W. B. and Dickinson, M. H. (2004). Force production and flow structure of the leading edge vortex on flapping wings at high and low Reynolds numbers. *J. Exp. Biol.* **207**, 1063-1072.

Dallmann, U., Herberg, T., Gebing, H. and Su, W. H. (1995). Flow field diagnostics: topological flow changes and spatio-temporal flow structure. *AIAA Paper*, 1995-0791.

Dudley, R. (1990). Biomechanics of flight in neotropical butterflies: morphometrics and kinematics. *J. Exp. Biol.* **150**, 37-53.

Dudley, R. (1991). Biomechanics of flight in neotropical butterflies: Aerodynamics and mechanical power requirements. *J. Exp. Biol.* **159**, 335-357.

Dudley, R. (2000). *Biomechanics of Insect Flight.* Princeton: Princeton Press.

Ellington, C. P. (1984a). The aerodynamics of hovering insect flight. II. Morphological parameters. *Phil. Trans. R. Soc. Lond.* **305**, 17-40.

Ellington, C. P. (1984b). The aerodynamics of hovering insect flight. III. Kinematics. *Phil. Trans. R. Soc. Lond. B* **305**, 41-78.

Ellington, C. P., Berg, C. V. D. and Willmott, A. P. (1996). Leading-edge vortices in insect flight. *Nature* **384**, 626-630.

Gordnier, R. E. and Visbal, M. R. (2003). Higher-order compact defference scheme applied to the simulation of a low sweep delta wing flow. *AIAA Paper*, 2003-620.

Henning, A., Rutten, M., Wagner, C. and Raffel, M. (2005). A stereo PIV investigation of a vortex breakdown above a delta wing by analysis of the vorticity field. *AIAA Paper*, 2005-4908.

Leibovich, S. (1984). Vortex stability: survey and extension. *AIAA J.* **22**, 1192-1206.

Liu, H., Ellington, C. P., Kawachi, K., Berg, C. V. D. and Willmott, A. P. (1998). A computational fluid dynamic study of hawk moth hovering. *J. Exp. Biol.* **201**, 461-477.

Maybury, W. J. and Lehmann, F.-O. (2004). The fluid dynamics of flight control by kinematic phase lag variation between two robotic insect wings. *J. Exp. Biol.* **207**, 4707-4726.

Norberg, R. A. (1975). Hovering flight of the dragonfly *Aeschna juncea* L., kinematics and aerodynamics. In *Swimming and Flying in Nature* (ed. T. Y. Wu, C. J. Brokaw and C. Brennan), pp. 763-781. New York: Plenum Press.

Perry, A. E. and Chong, M. S. (2000). Interpretation of flow visualization. In *Flow Visualization: Techniques and Examples* (ed. A. J. Smits and T. T. Lim), pp. 1-26. London: Imperial College Press.

Srygley, R. B. and Thomas, A. L. (2002). Unconventional lift-generating mechanisms in free-flying butterflies. *Nature* **420**, 660-664.

Su, W. H., Liu, M. J. and Liu, Z. Z. (1990). Topological structures of separated flows about a series of sharp-edged delta wings at angles of attack up to 90-deg. In *Proceedings of the IUTAM Symposium* (ed. H. K. Moffatt and A. Tsinober), pp. 395-407. Cambridge: Cambridge University Press.

Sun, M. and Tang, J. (2002a). Lift and power requirements of hovering flight in *Drosophila virilis*. *J. Exp. Biol.* **205**, 2413-2427.

Sun, M. and Tang, J. (2002b). Unsteady aerodynamic force generation by a model fruit fly wing in flapping motion. *J. Exp. Biol.* **205**, 55-70.

Taylor, G. S. and Gursul, I. (2004). Buffeting flows over a low-sweep delta wing. *AIAA J.* **42**, 1737-1745.

Wu, J. H. and Sun, M. (2004). Unsteady aerodynamic forces of a flapping wing. *J. Exp. Biol.* **207**, 1137-1150.